HHS Public Access

Author manuscript

Nat Mater. Author manuscript; available in PMC 2024 July 01.

Published in final edited form as:

Nat Mater. 2024 January ; 23(1): 139–146. doi:10.1038/s41563-023-01680-4.

Self-rectifying magnetoelectric metamaterials for remote neural stimulation and motor function restoration

Joshua C. Chen[†,1], **Gauri Bhave**[†,2], **Fatima Alrashdan**[2], **Abdeali Dhuliyawalla**[2], **Katie J. Hogan**[1,3], **Antonios G. Mikos**[1], **Jacob T. Robinson**[*,1,2,4,5]

[1]Department of Bioengineering, Rice University, Houston, TX, USA

[2]Department of Electrical and Computer Engineering, Rice University, Houston, TX, USA

[3]Medical Scientist Training Program, Baylor College of Medicine, Houston, TX, USA

[4]Applied Physics Program, Rice University, Houston, TX, USA

[5]Department of Neuroscience, Baylor College of Medicine, Houston, TX, USA

Abstract

Magnetoelectric materials convert magnetic fields to electric fields. These materials are often used in wireless electronic and biomedical applications. For example, magnetoelectrics could enable remote stimulation of neural tissue, but the optimal resonance frequencies are typically too high to stimulate neural activity. Here, we describe a self-rectifying magnetoelectric metamaterial for precisely timed neural stimulation. This metamaterial relies on nonlinear charge transport across semiconductor layers that allow the material to generate a steady bias voltage in the presence of an alternating magnetic field. We generate arbitrary pulse sequences with time-averaged voltage biases in excess of 2 V. As a result, we can use magnetoelectric nonlinear metamaterials (MNMs) to wirelessly stimulate peripheral nerves to restore a sensory reflex in an anesthetized rat model and restore signal propagation in a severed nerve with latencies of less than 5 ms. Overall, these results showing the rational design of magnetoelectric metamaterials support 26 applications in advanced biotechnology and electronics.

Remote stimulation of neural activity would enable less invasive medical therapies and improve our ability to study neuroscience in freely behaving animals. Magnetic fields are a promising candidate for remote control of neural activity because these fields can pass losslessly through air and penetrate deep into the body. However, the cells and proteins in our body have very weak magnetic properties; thus, for magnetic fields to stimulate a biological response, researchers typically either use high-field strengths in excess of 1 T that

[*]Corresponding author: jtrobinson@rice.edu.
[†]These authors contributed equally to this work

Author contributions:

J.C.C., G.B., and J.T.R. conceived of the magnetoelectric nonlinear metamaterial concept. J.T.R. supervised the research. J.C.C. and G.B. completed majority of the experiments and data collection. F.A., A.D., K.J.H., and A.G.M. assisted with material characterization. J.C.C., G.B. and J.T.R. prepared the manuscript with input from all the authors. F.A. provided review and editing of the manuscript.

Competing interests: JTR is a co-founder of Motif Neurotech, Inc., where he has equity stake and receives compensation. The views presented here should not be considered as endorsements of any specific product or company. The remaining authors declare no competing interests.

are generated by pulsed magnetics (1) or they use magnetic materials that convert a weak magnetic stimulus (typically less than 100 mT) into a form of energy that can stimulate nearby cells. Indeed, this materials-based approach offers superior selectivity because one can target a specific area for stimulation by limiting the location of the magnetic materials, or one can combine the magnetic materials with genetically modified cells to achieve cell type-specific neural stimulation (2–7). A materials-based magnetic stimulation technique that could achieve millisecond timing would enable numerous neurotherapeutic and research applications that require neuromodulation to be precisely timed with sensory stimuli and behavior (8,9); however, existing magnetic materials have fallen well short of millisecond temporal precision. For example, magnetic heating of superparamagnetic nanoparticles can stimulate neurons that express thermoreceptors (2–5) with behavioral response times approaching 500 ms (6) or trigger the release of drugs that cause a behavioral response with a latency of several seconds (7). Mechanical displacement of magnetic nanoparticles can also stimulate neural activity via mechanoreceptors (10,11), but the response times are several seconds in vivo (12). Magnetoelectric (ME) nanoparticles have also been used for remote neuromodulation with the thought that the material could convert an applied magnetic field to an electric field to directly activate voltage gated ion channels. However, the experiments involving ME nanoparticles show relatively long latencies ranging from a few hundred milliseconds to a few seconds (13,14), suggesting they are not directly driving action potentials on-demand. This long latency is likely because the ME nanoparticles are driven at 150 Hz, which is far from their resonance frequency. This frequency difference results in relatively small electric fields due to the reduced magnetoelectric coupling coefficient that is observed off resonance. Indeed, the conversion between magnetic and electric field characterizes as “α” (where $E = \alpha H$) increases more than 100-fold when the applied magnetic field matches a mechanical resonant mode of the material and more than 10^6-fold when compared to off-resonant magnetic nanoparticles (14,15). For materials less than 5 mm in length, the lowest resonance frequency is typically larger than 100 kHz which is too fast to directly stimulate neural activity due to the cell’s intrinsic low-pass filtering (16). Thus, for frequencies much higher than the low-pass cutoff frequency of the cell membrane, which is around 1 kHz, self-rectification is necessary to efficiently activate voltage-gated ion channels. As a result, ME materials have only achieved neural stimulation with millisecond latencies when they are combined with electronic circuits that convert the high-frequency ME response to a low-frequency electrical stimulus (17–20). We hypothesized that we could achieve millisecond-timed neural stimulation if we used a ME material with a nonlinear ME coupling coefficient α. A nonlinear α could allow self-rectification in the ME response. In fact, nonlinear charge transport has been demonstrated in similar material systems resulting in large 2nd order nonlinearities (21–23). In such a nonlinear ME material, self-rectification would convert an alternating current (AC) driving magnetic field to a direct current (DC) electric field by simply pulsing the AC carrier wave (Fig. 1A). This DC electric field should allow fast stimulation of voltage gated ion channels.

Because there have been no reports of ME materials with large nonlinear coefficients in natural materials, we were inspired by the field of metamaterials to engineer a composite material whose overall ME coupling coefficient would display a strong nonlinearity. Table 1 shows several other metamaterials where the conversion between fields or forces is

described by a material property that is not observed in nature, but can be engineered by a combination of constituent materials or components (24). We hypothesized that we could create a self-rectifying magnetoelectric nonlinear metamaterial (MNM) by adding a nonlinear charge transport layer to a ME laminate (Fig 1B). This composite material would thus have a nonlinear magnetoelectric coupling coefficient α that describes the relationship between the applied magnetic field (H) and the induced electric potential (V) ($V = \alpha H$) (Fig 1C).

Nanofabricated layer enables nonlinear metamaterial

To create this self-rectifying MNM we added a nanoscale rectifying electron transport (RET) layer to the ME laminate that consists of a trilayer laminate with a piezoelectric layer made of PZT at the center of two magnetostrictive layers made of Metglas (25) (Supplementary Figure 1). The RET was added by depositing 130 nm of ZnO and 40 nm of HfO_2 to create a thin film stack that acts as a diode for charge carriers moving through the material (26,27) (Fig. 2D). Our rationale for this design was to break the symmetry in the voltage response to positive and negative magnetic fields. In this way we could create a strongly non-linear ME coupling coefficient that would result in self-rectification (Fig. 1C). We chose ZnO for the RET layer because it has been used previously to fabricate diodes (28,29) and we can deposit it at low temperatures (100 °C) without the need to perform chemical etching, which allows monolithic integration with ME laminates. To improve the rectifying characteristics of the structure, we controlled the electron concentration in the ZnO layer by using Atomic Layer Deposition (ALD) at a low temperature with regulated precursor flow rates (30,31). We also deposited a passivating HfO_2 layer to further improve rectification characteristics by preventing reverse current (Fig 2E) (see methods). This thin-film stack works exclusively in Space Charge Limited Current (SCLC) mode thus overcoming the drawbacks of diodes that rely on tunneling currents (Supplementary Figure 2B). Characterization of the ZnO/HfO_2 stack showed typical diode rectification properties with an ideality factor of 6.8 and a rectification ratio of 95.38 (see Methods, Supplementary Figure 2A). With the addition of the RET, we can model the MNM material as a clamper circuit (Fig 1D bottom inset), which shows a nonlinear ME response.

When we characterized the ME coupling coefficient of the MNM we indeed found a strong 2nd and 3rd order nonlinearity (Fig. 1D). Plotting the induced voltage across the MNM as a function of the amplitude of the applied magnetic field between −0.5 mT and 0.5 mT (Fig 1D, blue dots) we see a nonlinear relationship that can be well-fit as a third order polynomial, where $V = \alpha_1 H + \alpha_2 H^2 + \alpha_3 H^3$ ($\alpha_1 = -7.75$, $\alpha_2 = 7.75$ and $\alpha_3 = 5.99$) (Fig. 1D, blue line). This is in stark contrast to unmodified ME laminates (Fig 1D, green dots) that are well fit by a linear relationship $V = \alpha_1 H$ ($\alpha_1 = 7.2405$) (Fig. 1D, green line) (see methods). In all cases, these experiments were performed with the alternating magnetic field frequency matching the fundamental resonant mode and under a DC magnetic field bias where the ME coefficient is known to achieve the maximum value (see Methods).

We confirmed that the nonlinear ME coupling coefficient is the result of the nonlinear RET by comparing the MNM response to the nonlinear transport across the RET layer (Fig. 2C). Figure S3A shows the I-V relationship measured from our RET, at the operational frequency

of 335 kHz, which is the mechanical resonant frequency of the MNM. We then used the linear H-V relationship measured in the ME laminate (Fig 1D) to convert the I-V curve in Supplementary Figure 3A, into an H-I curve in Supplementary Figure 3B (see Methods). We separately measured the H-I relationship of the MNM by varying the amplitude of the alternating magnetic field (H) while measuring the current (I) across a load resistor (R_L) (Fig. 3C). When we normalized the H-I curve measured in the MNM and computed H-I curve for the ME+RET we find that both H-I relationships show similar nonlinear relationships (Fig. 2C). These results confirm that the nonlinearity observed in the MNM can be explained by the non-linear charge transport across the RET layer (Fig. 2C).

Metamaterial generates DC bias under a pulsed magnetic field

When we apply an AC magnetic field at the mechanical resonant frequency, we find that the MNM shows self-rectification, which is key for precisely timed neural stimulation (Fig. 2B). The red line shows a 200 μs window sliding average of voltage waveform, which reveals a 1.7 V bias voltage develops across the MNM but not across the ME film (Fig 2A) when a magnetic field is applied (see methods). These data also show that by pulsing the AC magnetic field we can generate a DC electrical stimulus. Figure 2A and 2B show the example of an arbitrary low-frequency pulse train using a 375 kHz carrier. Thus, we can generate a low-frequency electrical stimulus using the high-frequency magnetic carrier signal. This ability to demodulate the high-frequency carrier to a low-frequency electrical impulse is what enables us to generate a waveform that can directly activate voltage gated ion channels that would otherwise not respond to a high-frequency alternating electric field.

MNM restores sensor motor reflex in rodent model

As a proof of principle, we demonstrate the capability of the MNM to restore a fast sensory motor reflex in an anesthetized rat. For this experiment we use the MNM to stimulate the sciatic nerve when we measure mechanical stimulation of the rat's foot using a force sensor (Fig. 3A). Under awake or lightly sedated conditions, rats display a sensory reflex where the leg muscle contracts producing a leg kick when the foot is pinched. (Supplementary Figure 4) When rats are fully anesthetized this sensory response is inhibited and the lack of this sensory motor reflex is often used to check whether the animal is fully anesthetized. To test if the MNM could function as part of a neuroprosthetic capable of restoring sensory motor reflexes, we programmed the magnetic field driver to stimulate the MNM at a 1 Hz frequency when a force sensor on the rat foot measures a mechanical stimulation. For these experiments, we placed a rat under anesthesia and surgically exposed the sciatic nerve (see methods). After isolating and lifting the sciatic nerve, we placed the MNM on the exposed nerve and applied a magnetic field with an external field generator at the skin's surface in response to a trigger from the force sensor on the foot of the rat (see methods) (Fig. 3A and Supplementary Figure 5). With the rat fully anesthetized we observed no EMG or leg kicks when we pinched the rat's foot. However, when we activated the MNM with a remote magnetic field pulse (1.5 mT, 1 ms) in response to the force sensor, we observed restoration leg kicks EMG signals when we pinched the toe demonstrating that MNMs can act as part of a neuroprosthetic system (Fig. 3B). We found that the MNM was capable of reliable stimulation at frequencies of 1, 2, and 10 Hz when driven at the

resonant frequency suggesting that these MNM could support a variety of neuroprosthetic applications that require millisecond timing. (Fig. 3C,Supplementary Figure 6). To confirm that the neural stimulation was the result of the selfrectifying MNMs and not the magnetic field stimulus, we detuned the magnetic field driver away from the resonance frequency by less than 5% and found that both the leg kicks and EMG responses vanished. (Fig. 3D) We also observed no leg kicks or EMG response when we stimulated a ME laminate at its resonance frequency (Fig 3E), confirming that the self-rectifying properties of the MNM is key to enabling rapid stimulation of neural activity. By changing the magnetic field strength, we can also tune the output voltage of the MNM. This tunability allowed us to map motor evoked potentials and demonstrated a sigmoidal muscle recruitment curve as shown in Fig 3F. To further explore the possibility of developing the MNM for longer term implantations and to validate wireless tissue penetration, we sought to demonstrate nerve stimulation in a closed wound model. Because our metamaterial composite utilizes electric fields to stimulate nerves, we insulated the layers with ~20 μm of Parylene-C to prevent shorting across the material stack. We originally chose ZnO as it was a wide band gap material that has been widely studied as a semiconducting material, specifically for thin film diodes. We found that this layer provided a good rectification ratio, however we found a relatively low yield of approximately 10%. As a result, for closed wound experiments we used an alternative RET layer consisting of a p-n diode fabricated by forming a heterojunction between p-Si and our previously used n-ZnO. With this material composition, we found approximately 80% yield with a larger DC bias of >2V which enables more robust wireless activation for fully implanted, closed-wound applications as shown in Fig 3G. Because magnetic fields are not attenuated by tissue, we were able to fully implant the MNM with a 3D printed nerve clip in a closed-wound model, and we measured EMG at the stimulation frequency of 1 Hz (Fig 3H, Supplementary Figure 7). A systematic exploration of the variety of RET layers is outside the scope of this work, but there are likely many alternative approaches which may produce improved performance. To further explore the potential of the MNMs as longer-term implants, we also tested the biocompatibility by culturing human embryonic kidney (HEK) cells with the insulated MNM for ~5 days to prevent overgrowth which would decrease cell viability. We tested the culture with a live dead assay and observed an 89% viability for cells cultured with the MNM which was comparable to the positive control at 85% viability (Supplementary Figure 8). We also tested a negative control that showed a 62% viability using a mixture of ionomycin and PMA which induces irreversible calcium influx (Supplementary Figure 8). Furthermore, we carried out a soak test in phosphate buffered saline at the physiological temperature of 37 °C. We observed that the material was able to maintain peak-to-peak voltage and DC bias up to 5 days before signs of degradation due to fluid ingress appeared (Supplementary Figure 9). Additionally, we implanted the MNM and a Polydimethylsiloxane (PDMS) control subcutaneously in rodents over three weeks and performed histological analysis (see methods). We monitored the wound healing process weekly and observed intact overlying skin with no dehiscence and minimal scarring at the incision site (Supplementary Figure 10). On Hematoxylin and Eosin (H&E) staining of the biopsied tissue from week 3, increased blood vessel and cellular infiltration compared to native undisturbed tissue were observed in the subcutaneous space. However, this increase occurred at similar rates for both MNM and PDMS implantation sites indicating a foreign body response independent of the material (Supplementary Figure 11).

Together these results show that encapsulating the MNM can render the material nontoxic and operational under physiological conditions. The longevity of these encapsulation layers will determine the overall lifetime of the device. Improved encapsulation will be needed for long-term operation, which could potentially be achieved with better insulation strategies such as inorganic coatings with Al_2O_3 or combination coatings of polyamide and parylene (32,33).

MNM bridges severed nerve gap with millisecond latencies

As another example of how the precisely timed MNM stimulation can support neuroprosthetic applications we used the MNM to restore nerve conduction across a severed rat sciatic nerve (Fig. 4). As shown in Fig. 4A, we used a pulse generator to stimulate upstream of the severed nerve with a 1 mA, 1 ms pulse and used a nerve cuff to record the nerve potential at this proximal end of the severed nerve (Supplementary Figure 12). We then used this voltage measured on the nerve cuff as a trigger for the magnetic field driver to activate an electrical pulse in the MNM powering a nerve cuff on the distal end of the severed nerve. In this way we use the MNM to bridge the nerve gap allowing the electrical signal to continue across the severed nerve relying on the short latency of the MNM to avoid significant signal propagation delay. (Fig. 4A, Supplementary Figure 14). We plot the applied and measured voltages in Fig. 4. We found that the MNMs successfully bridge the sciatic nerve gap and enable nerve signals to activate the distal muscle groups with latencies of less than 5 ms (Fig 4C). This response time is approximately 120-fold faster than any previously reported remote neural stimulation using magnetic materials (6). Unlike existing magnetic materials used for neural stimulation, we show high temporal control with our MNMs, demonstrated by both the short latency between pulse generator and the EMG response (4.06 +/− 0.21 ms) as well as the ability to drive neural responses at frequencies up to 10 Hz (Fig. 4C, Supplementary Figure 6). Furthermore, the latency between the pulse generator and the MNM across the nerve gap is only ~175 us. These fast latencies and associated higher stimulation bandwidths are important for many neurotherapeutic applications such as neuroprosthetics where sensory information needs to be quickly transmitted from a prosthetic (as demonstrated with the force sensor) or for bridging a signal propagation across a severed nerve.

The ability to engineer nonlinear magnetoelectric effects not previously observed in ME materials is the key element that enables these magnetic metamaterials to achieve precisely timed stimulation of neural activity. An additional advantage is that we achieve this precise remote stimulation of neural activity without any genetic manipulation of the target tissue, which eases the path for potential clinical applications. Compared to other magnetic materials for neural interfaces that can be as small as 10 nm in diameter (2–6,13,14), the MNMs demonstrated here range in size from millimeters to centimeters in length which match the length scales of the rat sciatic nerve and other peripheral nerve stimulators that rely on functional materials (34). However, the thin-film stack used to create the MNMs here resemble chemical synthesis processes that could potentially support production of micro- and nano-scale materials. In fact, when we measured the self-rectified bias potential of our mm-scale MNMs as a function of material size we found that the bias potential remained relatively constant (Supplementary Figure 13). These data suggest that micro and

nanoscale versions of the MNM may also have similarly large self-rectification properties. Furthermore, the nonlinearities introduced by the RET layer are highly reproducible with each batch showing some degree of rectification. However, in our current fabrication process we observe batch variation in DC voltage produced by the self-rectification (Supplementary Figure 14). With further improvements in more advanced and tightly controlled fabrication steps, it may be possible to reduce the variabilities. Furthermore, MNMs only require < 1.5 mT magnetic fields which causes undetectable and negligible heating from both the MNM and the coil (Supplementary Figure 15). Given this new metamaterial concept, more work is needed to develop theoretical treatments to describe the metamaterial properties. The MNM we demonstrate here relies on a nonlinear charge transport layer that affects the relationship between the electric displacement and electric field. This nonlinear effect is likely to be best represented as an effective nonlinear permittivity, but a theoretical description of MNMs is not fully developed here, and alternative electronic elements could be used to create MNMs with a variety of linear and non-linear effective dielectric properties. Additionally, other types of nonlinearities could be introduced by engineering different aspects of the magnetic-to-electric transduction pathway. For example, for strain-mediated magnetoelectric materials like those described here, it may be possible to engineer the mechanical properties of the laminate and introduce nonlinearities in the magnetoelectric coupling by drawing from work in acoustic metamaterials (35). One characteristic of the MNMs is the fact that they are not symmetric magnetoelectric metamaterials. Specifically, there is nonlinear magnetoelectric coupling between an applied magnetic field that induces an electric field, but not vice versa. In this case the magnetoelectric coupling equations can be written as Eq. 1 and Eq. 2 where only α_{HE} has non-zero components in the non-linear expansion. This concept is similar to existing optical metamaterials (36,37).

$$E = \alpha_{HE_1} H + \alpha_{HE_2} H^2 + \alpha_{HE3} H^3$$

Eq 1.

$$H = \alpha_{EH} E$$

Eq 2.

A potential concern for chronic biotechnology applications is encapsulation of the MNM to avoid damping the ME coefficient, and some materials like PZT layer which contains lead, may need to be substituted for more inert piezoelectric materials like AlN or PVDF. In summary, we show that it is possible to rationally design metamaterials that convert magnetic fields to electric fields to overcome challenges in neurotechnology, but this framework for metamaterial design can likely be applied to diverse applications in sensing, electronics, and memory that rely on manipulating magnetic and electric fields in miniature materials.

Methods:

Fabrication of ME:

The ME material was fabricated by sandwiching a piezoelectric material between two sheets of a magnetostrictive material. A sheet of Metglas (23 μm) was first cleaned using Isopropyl Alcohol (IPA). The Hardman double bubble 2-part epoxy was then applied to the Metglas sheet and a sheet of lead zirconate titanate (PZT – 5A, 250 μm) was placed on top to form the composite material. This was left to dry for 5 minutes at room temperature. Another sheet of Metglas cleaned with IPA was bonded to this laminate, using the same epoxy to form a sandwich structure. The films were then cut to a desired size using a femtosecond laser cutter. Conductive Ag epoxy is used to connect 30 AWG wire to make electrical contact with the ME film so that the voltage could be tested. The same method was used to fabricate 2-layer ME materials where a sheet on Metglas was attached to a PZT sheet using the method described above (17). We characterized the two- and three-layer ME composites and found that they have qualitatively equivalent characteristics (Supplementary Figure 16Aand Fig 1D-green dots).

Fabrication of MNM:

For fabrication of the MNM, a Metglas sheet was first plasma cleaned for 2 minutes. One side of the Metglas was then masked and on the other side 50 nm of Pt was deposited by sputtering using (AJA ATC Orion sputter, MA, USA) at 15 W in the presence of 30 sccm Argon for 20 minutes. Following this, 40nm of HfO_2 was deposited as the passivating layer. Atomic Layer Deposition (Cambridge Ultratech Savannah 200) was used to get a conformal layer. Deposition was done at 150C using Tetrakisdimethylamido (TDMA) and H_2O. On top of this, ALD was used to deposit 130nm of ZnO with the diethyl zinc (DEZ) precursor and H_2O. This deposition was done at 100C, with precursor pulses of 0.015 seconds for DEZ and 0.015 seconds for H_2O and a 45s reaction time between pulses to control the charge carrier concentration in this layer to achieve the self-rectification properties. The alternative p-n RET layer was fabricated by depositing 50 nm of Al using 50 W in the presence of 30 sccm Argon for 15 minutes by sputtering using the AJA ATC Orion sputter. Then, 500 nm of a p-Si was deposited using e-beam evaporation. Deposition of 100 nm of ZnO was the same recipe as above. To allow for more misalignment and distance tolerance in the closed wound model, we stacked two ME laminates in series with the RET layer. For both the Schottky and p-n RET layers, we experimentally optimized the thicknesses of the layers as well as deposition temperature of the ZnO layer. We evaluated the nonlinear effect on the voltage bias and peak-to-peak voltage for each of these conditions as shown in Supplementary Figure 17. The masking on the Metglas was then removed and the pristine side of this Metglas was attached using the non-conductive epoxy, to a laminate of Metglas (23 μm) and PZT (250 μm) fabricated using the same methods as those used to make the 2-layered ME material and was cut to an appropriate size. Silver epoxy was used as the metal contact to connect the ZnO to the bottom of the ME film using polyamide tape to insulate the remaining stack of materials. Figure 3 (left) shows the cross section of the entire material. Figure 3B (right) shows a zoom in on a false-colored SEM of the cross section of the deposited Schottky RET layers and the full view of both types of RET layers are shown in Supplementary Figure 18. Furthermore, we performed XRD on both stacks to characterize

the RET layers where peaks were seen at θ = 31.77, 34.34, and 36.18 which correspond to (100), (2) and (101) of ZnO. These peaks are normally observed in ZnO thin films deposited using ALD at low temperatures (41). For the Schottky RET, a clear Pt peak was observed along with HfO_2 peaks that overlap with ZnO due to its oxide nature (Supplementary Figure 19A) (42). For the p-n RET, we observe an extra peak at 56.61 which corresponds to both ZnO (110) and Si (211) (43).

MNM Characterization:

The fabricated RET stack follows the typical curves of a Schottky diode (Supplementary Figure 2A) with a turn-on voltage of 0.3V. We measured the I-V curves using a source meter (Keithley 2400). From the I-V curves, we calculated the rectification ratio. We obtained a rectification ratio of 95.38 at 10V. This was calculated by using the equation RR(V)=I(V)/I(-V). This is comparable with the rectification ratios of commercial silicon diodes which are between 105 and 108. We then fit the Shockley equation to our RET I-V curves as follows:

$$I = I_s\left(e\left(\frac{qV}{nKT}\right) - 1\right)$$

Where, V is the applied voltage, T=298K is the absolute temperature (room temperature), K is the Boltzmann constant and q is the charge of an electron.

By fitting the Shockley diode equation to the I-V curves we found that the RET had an ideality factor of 6.8, and a Saturation current Is=1.69 $\times 10^{-8}$ which is comparable to other thin film diodes (44). These values clearly indicate that the RET layer forms a Schottky diode that modifies the effective permittivity within the MNM to provide the self-rectifying characteristics. We plotted the log I-log V curves (Supplementary Figure 2B). The linear curve in the positive region and the non-linearity in the negative region shows that the electron transport in this material occurs through the SCLC mechanism and tunneling currents are restricted in the negative bias mode (25). To additionally verify the rectifying characteristics, we connected the MNM material in series with a signal generator (BK Precision 4052) and measured the output of the test circuit on an oscilloscope (Tektronix TBS1052B). We see a rectified output voltage for an input sine wave (Supplementary Figure 16B). To further verify that the ZnO/HfO_2 combination and specific fabrication methodology results in the obtained rectification, we fabricated a structure with Al_2O_3 as the charge transport layer. We found no rectification as seen from the I-V curves (Supplementary Figure 16D).

To determine whether our material or coil would heat up during operation, we used a FLIR Infrared thermal camera to record the MNM being pulsed at 10 Hz with 1 ms pulse widths for 3 minutes. This demonstrated negligible heating from both the coil and the MNM (Supplementary Figure 15).

MNM Live Dead:

HEKs were cultured with the encapsulated MNM for 5 days. We used a 'viability/ cytotoxicity assay kit for animals' from Biotium. For the negative control, we used 5 μM ionomycin + 10 ng/uL PMA concentrations to induce calcium influx.

ME and MNM coupling coefficient:

To calculate the ME and MNM coupling coefficients, we used a 5 mm × 2 mm ME and MNM films with a mechanical resonance frequency of 345 kHz and 335 kHz respectively. The films were wirelessly driven with a magnetic field at their respective resonant frequencies. We varied the amplitude of the AC magnetic field between 0 to 0.5mT and used an oscilloscope (Tektronix TBS1052B) to measure the output maximum and minimum voltage values, which correspond to the maximum and minimum applied magnetic field. The graph of measured output voltage and applied magnetic field is plotted in Fig 1D (bottom) for both ME and MNM. We then used a polynomial function to fit the measured curves to obtain the coupling coefficients for ME and MNM. We also did the same measurement for MNM between −1.5mT to 1.5mT, since we used a 1.5mT field for the in vivo experiments. We see that the MNM material saturates beyond a certain magnetic field strength, however the trend of the output voltage follows the nonlinearity introduced by the diode layer. The results are shown in supplementary Supplementary Figure 16C.

ME and MNM H-I curves:

To compare the characteristics of ME and MNM, and to verify that the nonlinear characteristics of MNM were a direct result of the addition of the RET, we first measured the I-V curves of the RET layer at the MNM operational frequency of 335 kHz. To do this, we used a signal generator (BK Precision 4052), connected to a separately fabricated RET layer with an external resistance of 470k ohm in series as shown in Supplementary Figure 3A (inset). We varied the input voltage and measured the current across the load resistance to plot the RET I-V curves in Supplementary Figure 3A. Then we fit the I-V curve to a 5th order polynomial that accurately captures the measured data. For the ME film, we mapped the applied magnetic field values to the film output voltage values using H-V curve (Fig. 1D) then we mapped these values to the output current of the ME film + RET using the 5th order polynomial of the RET IV curve. The ME H-V curve from Fig 1D was then plotted as a function of this fit. The curve obtained through this is plotted in Supplementary Figure 3B. This curve represents the output current measured when the output voltage obtained from the ME material is applied as an input to the RET. We then measured the H-I curve of the MNM by measuring the current across a 470 kΩ resistance while applying a resonant magnetic field to the MNM. We compare the curves in Supplementary Figure 3B and Supplementary Figure 3C in Fig 2C.

Magnetic Field Transmitter:

A custom magnetic field driver using an H-bridge topology with SiC based MOSFETs (APEX SA310KR) was used to power our magnetic coils. This driver can handle output currents up to 30A and up to 400 kHz frequencies. For smaller films and higher frequency magnetic fields, we used a GaN based field driver that supported >10 MHz switching

frequencies (45). The entire transmitter system included the use of an Arduino that was programmed through USB from a laptop. The microcontroller sent two signals to the driver to control the H-bridge in order to drive biphasic square pulses through the resonant coil. The system included a 30-turn coil with an inner diameter of 17 mm, wrapped with 30 AWG wire.

In vivo biocompatibility test:

All procedures used in this *in vivo* biocompatibility assay complied with the National Institutes of Health standards and were approved by the Animal Care and Use Committee of Rice University (Protocol #IACUC-20–181). Three rats were chronically implanted with a Parylene-C encapsulated MNM on the right side of the lower back and a PDMS sham on the left side of the lower back. PDMS was chosen as an inert and biocompatible material. A three-millimeter incision was made to access the subcutaneous space where both implants were placed. 3–0 Vicryl sutures were used to close the wounds. Each week, one rat was sacrificed to observe the wound healing process and retrieve the implanted materials (Supplementary Figure 10). In the third week, the last rat was sacrificed, implants retrieved, and tissue biopsies were taken using a 6 mm biopsy punch at the site of the implant. The tissue samples were then soaked in 10% formalin for ~20 hours. Afterward, the samples were processed for six hours in 15% w.t. sucrose solution as a cryoprotectant before being moved into a 30% w.t. sucrose solution overnight. Once the samples were fully processed, they were embedded in Tissue-tek O.C.T. compound before being processed into ~15 μm slices with a cryostat. H&E staining was applied to visualize the tissue structure and cells within the sample.

In vivo Rat Sciatic Nerve:

All procedures carried out in this research complied with the National Institutes of Health standards and were approved by the Animal Care and Use Committee of Rice University (Protocol #IACUC-20–181). The MNMs were used to stimulate the sciatic peripheral nerve of adult (2–5 months) Long Evans rat models. Successful stimulation of the rat hind legs by the MNMs were confirmed with recorded EMG and observable leg kicks. For the surgical procedure, the animals were placed under anesthesia with an induction chamber with 5% isoflurane in oxygen at a flow rate of 1–2 liters per minute. When the rat was unconscious and areflexic, confirmed with toe pinches, the animal was transferred to a 40°C heated pad with a nose cone to provide ~2% isoflurane. Meloxcam 2 mg/kg SC and Ethiqa XR SC 0.65 mg/kg were administered to the rat prior to shaving around the surgical site. The site was then sterilized using iodine swabs before a semi-circular incision was cut across the hip of the rat. The fascial plane between the gluteus maximus and anterior head of the bicep femoris was dissected to expose the peripheral nerve.

Underlying connective tissue was carefully cut to isolate the sciatic nerve. The MNM is then placed directly on the nerve and held in place with a nerve clip. The magnetic coil is brought to the surface of the skin where the MNM is at an implant depth of > 1 cm (Supplementary Figure 20). EMG is recorded through two needle electrodes on the subplantar regions with a reference electrode connected to the main body of the rat. The recording system included a DAQ and dual bioamplifier (ADsystems) sampling at 1 kHz. The data was preliminarily

observed through LabChart before exporting to MATLAB for processing. Upon completion of the experiments, the animals were immediately euthanized under proper guidelines.

For the experiments, the MNMs were made with 3 different dimensions-- sample 1: 10 × 5mm, sample 2: 5 × 3mm and sample 3: 3 × 2mm. The bottom Metglas layer was extended for the extra surface area to deposit electrodes on the same plane of the material. The three samples for wireless stimulation of the rat sciatic nerve were used by bringing the silver epoxy pads fabricated on the MNM surface into contact with the sciatic nerve (Fig. 3A inset) and the MNMs were wirelessly driven by magnetic fields at 1.5mT and a ~6–8 mT DC field from a bias magnet to obtain maximum voltages (Supplementary Figure 6). The DC field is used to maximize the magnetostriction in the MNM laminate. It could easily be implemented with a smaller sized magnet or electromagnetic coil and this full transmitter system has been shown for potential wearable applications (19). For all three samples (Sample1: 100KHz, Sample 2: 242KHz, Sample 3:335Khz), we observed leg kicks and recorded the EMG response. Additional control data was obtained to verify that the MNMs only work at the mechanical resonant frequency of the material. For this, MNMs were driven off-resonance (Sample 1: 90KHz, Sample 2: 230KHz, Sample 3: 330 kHz). We observed no leg kicks and no EMG signal was obtained with off resonance stimulation (Supplementary Figure 21B). To calculate the response latency, we used MATLAB 2017 to quantify the time difference between the initial PG pulse and the first peak of the EMG response. These experiments were performed with MNMs of various sizes ranging between 3 mm and 10 mm in length with resonance frequencies varying between 100 to 375 kHz. The latencies and EMG responses were similar to those evoked by direct electrical stimulation with wired electrodes (Supplementary Figure 21C). The artifacts for each condition were labeled where the large monophasic artifact in Supplementary Figure 21A/B are due to interference from the resonant magnetic coil picked up by the EMG electrodes. In contrast, when the pulse generator stimulus is far from the body, we observe a smaller stimulus artifact that is coupled from the stimulating cuff through the tissue as can be seen in Supplementary Figure 21C.

For the severed nerve experiment, the sciatic was cut using surgical shears. Stimulating electrodes in a 3D printed nerve cuff were hooked up to the ADsystems pulse generator. A stimulating pulse of 1 mA with 1 ms pulse width was applied upstream of the proximal nerve ending. Recording electrodes in a 3D printed nerve cuff were then used to measure resulting potential at the severed proximal end of the nerve. This recorded voltage was then amplified and used as a trigger to initiate a single millisecond long magnetic field pulse that would power the MNM connected to stimulating nerve cuff electrodes on the distal severed nerve ending (Supplementary Figure 12). EMG electrodes were placed in the bicep femoris of the rat to record resulting muscle activity. We further tested different pulse generator stimulus amplitudes and observed varying recorded nerve potentials (Supplementary Figure 22).

For the closed wound model, we 3D printed a nerve clip using a Projet MJP 2500 using standard VisiJet M2R material. This nerve clip helped to secure good contact between the MNM and the sciatic nerve. Once the system was secured on the nerve, we closed the

muscle and skin with 5–0 Vicryl suture (Cat. J303H Ethicon). In Fig 3G, we can see the feedback wires protruding out of the wound, EMG electrodes, and excess suture.

To test the on and off resonant controls using the ME laminates, polyamide was used to insulate one edge of the film before adding the conductive epoxy. One conductive epoxy electrode was placed in the center of the ME film while the other electrode on the reverse side was deposited in the center and wrapped around the edge of the insulated film so that both electrodes would reside on the same side and plane. The ME laminates were driven at 335 kHz on resonance and at 325 kHz for the off resonant control by bringing the resonant coil to the surface of the rat. This resulted in a recorded artifact pulse but no observable leg kick or recorded EMG. We further verified that the physiological response was indeed a function of the rectification and modulation of the high carrier frequency to the lower pulsed frequency. In this case, we powered Pt electrodes that were brought into contact with the sciatic nerve using a wired ME film (5 mm × 3 mm) driven with a 245 kHz magnetic field. When we pulsed our magnetic field at 1 Hz with a 1 ms pulse width, we observed no response. Upon adding a commercial diode in parallel with the ME material, we observed leg kicks as well as recorded EMG signals that corresponded with the applied stimulation pulses. (Supplementary Figure 23)

In Vivo experiment for sensory reflex restoration:

The rats were induced under isoflurane with the same protocol mentioned above in the general rat procedure. A control experiment was run where the isoflurane concentration is reduced from the normal 2% to 0.5% to restore the toe pinch reflex response. A force sensor (Tekscan Flexiforce 101) was placed on the foot of the rat and used to visualize the toe pinch force and resulting EMG response was recorded from the femoris muscle of the rat (Supplementary Figure 4). The force sensor voltage read out saturates at 5V which is the voltage rail on the amplifier circuit. The isoflurane was then increased back to the usual 2% where the toe pinch test was executed and no EMG and muscle activation was observed, thus indicating a fully anesthetized animal. The same surgical procedure was then carried out to expose the sciatic nerve. A noninverting amplifier (TL061CP) was used to amplify the sensed voltage. The Arduino teensy was then configured to initiate 1 Hz stimulation when the sensor voltage reached a threshold. Occasionally, there would not be a resulting MNM voltage upon toe pinch as can be seen in Fig. 3B, this is due to slight misalignment of the transmitter to the metamaterial and thus not inducing a high enough voltage. All of the data in this paper showing successful nerve stimulation in rodents measured by EMG was done across n = 6 rats. Rats A, B, C were used in Figure S6. Rat D was used for both the sensorimotor restoration assay and severed nerve assay. Rat E was used for the closed-wound fully implanted study. Rat F was used to replicate the sensorimotor restoration and severed nerve assay shown in the supplemental videos. Each stimulation trial was able to be replicated more than three times. For both *in vivo* trials, no statistical methods were used to pre-determine sample sizes nor randomization methods used but our sample sizes are similar to those reported in previous publications (34). Data collection was not performed blind to the conditions of the experiment and no animals/data points were excluded.

Data availability

All relevant data supporting the results of this study are presented in the manuscript or the Supplementary Information. Raw data are available at https://osf.io/yr78v/

Code availability

Custom code used in this study is available at https://osf.io/yr78v/

Supplementary Material

Refer to Web version on PubMed Central for supplementary material.

Acknowledgments:

We would like to acknowledge Amanda Singer, Anne Tuppen, Matthew Parker, and Vishnu Nair for their useful discussions on magnetoelectrics. We would also like to acknowledge Edwin C. Lai for his assistance with rat nerve surgeries, Samantha Coffler for her assistance with the biocompatibility assay, and Aaron Bayles for his assistance with XRD. We also thank the staff at the Shared Equipment Authority (SEA) at Rice, Tim Gilheart, Jing Guo, James Kerwin, Hua Guo for their assistance and excellent discussions. Equally contributing authors are allowed to list their name first on their CV's.

Funding:

National Science Foundation ECCS-2023849 (GB, JCC, FA, JTR)

National Institutes of Health U18EB029353 (GB, JCC, FA, JTR)

National Institutes of Health F31 DE030333 (KJH, AGM)

References

1. Hallett M. et al. Transcranial magnetic stimulation and the human brain. Nature, 406(6792), 147–150 (2000) [PubMed: 10910346]
2. Chen R. et al. , Wireless magnetothermal deep brain stimulation. Science. (2015)
3. Huang H. et al. , Remote control of ion channels and neurons through magnetic-field heating of nanoparticles. Nature Nanotechnology. 5, 602–6 (2010).
4. Munshi R, Pralle A, Remote modulation of neuronal cells in the brain, Nature Materials vol. 20, p. 912–913 (2021) [PubMed: 34188201]
5. Moon J. et al. , Magnetothermal multiplexing for selective remote control of cell signaling. Adv. Funct. Mater 30, 2000577.(2020)
6. Sebesta C, et al. , "Sub-second multi-channel magnetic control of select neural circuits in 388 behaving flies", Nature Materials (2022)
7. Rao S. et al. , Remotely controlled chemomagnetic modulation of targeted neural circuits. Nature Nanotechnology, 14(10), 967–973. (2019)
8. Boyden ES et al. , Millisecond-timescale, genetically targeted optical control of neural activity. Nature Neuroscience, 8(9), 1263–1268. (2005) [PubMed: 16116447]
9. Bhave G. et al. , Distributed sensor and actuator networks for closed-loop bioelectronic medicine, Materials Today, 46, 125–135. (2021) [PubMed: 34366697]
10. Gregurec D. et al. , Magnetic Vortex Nanodiscs enable remote magnetomechanical neural stimulation. ACS Nano, 14, 8036–8045, (2020) [PubMed: 32559057]
11. Dobson J. et al. , Remote control of cellular behaviour with magnetic nanoparticles. Nature Nanotechnology, 3(3), 139–143. (2008)

12. Lee J. et al. , Non-contact long-range magnetic stimulation of mechanosensitive ion channels in freely moving animals. Nature Materials, 20(7), 1029–1036. (2021) [PubMed: 33510447]
13. Nguyen T. et al. , In Vivo Wireless Brain Stimulation via Non-invasive and Targeted Delivery of Magnetoelectric Nanoparticles. Neurotherapeutics (2021).
14. Kozielski K. et al. , Nonresonant powering of injectable nanoelectrodes enables wireless deep brain stimulation in freely moving mice. Science Advances, 7 (2021)
15. Tu C. et al. , Mechanical-Resonance-Enhanced Thin-Film Magnetoelectric Heterostructures for Magnetometers, Mechanical Antennas, Tunable RF Inductors, and Filters, Materials (Basel). 12(14):2259 (2019) [PubMed: 31337062]
16. Grossman N. et al. , Noninvasive Deep Brain Stimulation via Temporally Interfering Electric Fields, Cell, 169, 6 (2017) [PubMed: 28340351]
17. Singer A. et al. , Magnetoelectric materials for miniature, wireless neural stimulation at therapeutic frequencies, Neuron 107, 631–643 (2020) [PubMed: 32516574]
18. Yu Z, et al. , “MagNI: a magnetoelectrically powered and controlled wireless neurostimulating implant, IEEE Transactions on Biomedical Circuits and Systems (TBioCAS), 14,6, pp. 1241–1252 (2020)
19. Alrashdan F. et al. Wearable wireless power systems for ‘ME-BIT’ magnetoelectric-powered bio implants, Journal of Neural Engineering, 18 (2021)
20. Chen JC et al. Wireless endovascular nerve stimulation with a millimeter-sized magnetoelectric implant, Nature Biomedical Engineering (2022)
21. Li Z. et al. In situ ZnO nanowire growth to promote the PVDF piezo phase and the ZnO-PVDF hybrid self-rectified nanogenerator as a touch sensor. Phys. Chem. Chem. Phys, 16, 5475–5479. (2014) [PubMed: 24515250]
22. Kang BJ et al. Ultrafast and low-threshold THz mode switching of two-dimensional nonlinear metamaterials, Nano Letters, 22, 5 (2022).
23. Misewich JA et al. Electrically induced optical emission from a carbon nanotube FET, Science, 300, 5620, 783–786, (2003). [PubMed: 12730598]
24. Lincoln R. et al. Multifunctional composites: a metamaterial perspective, Multifunctional Materials, 2, (2019).
25. Cuong TD, et al. Giant magnetoelectric effects in serial-parallel connected Metglas/PZT arrays with magnetostrictively homogeneous laminates, Journal of Science: Advanced Materials and Devices, 5,3, pp. 354–360 (2020)
26. Park Y, et al. , Unidirectional oxide hetero-interface thin-film diode, Appl. Phys. Lett 107, 143506 (2015)
27. Krajewski TA, et al. Hafnium dioxide as a passivating layer and diffusive barrier in ZnO/Ag Schottky junctions obtained by atomic layer deposition, Appl. Phys. Lett 98, 263502 (2011)
28. Brillson LJ and Lu Y, ZnO Schottky barriers and Ohmic contacts, Journal of Applied Physics 109, 121301 (2011)
29. Mondal S, et al. , Preparation of ZnO Film on p-Si and I-V Characteristics of p-Si/n-ZnO, Materials Research. 16(1): 94–99 (2013)
30. Guziewicz E, et al. , ALD grown zinc oxide with controllable electrical properties, Semicond. Sci. Technol 27, 074011, (2012)
31. Jeon et S. al. Structural and electrical properties of ZnO thin films deposited by atomic layer deposition at low temperatures, Journal of The Electrochemical Society, 155,10, H738-H743, 443 (2008)
32. Xie X. et al. Long-term Reliability of Al2O3 and Parylene C Bilayer Encapsulated Utah Electrode Array Based Neural Interfaces for Chronic Implantation, Journal of Neural Engineering, 11 (2014)
33. Pak A. et al. Thin Film Encapsulation for LCP-Based Flexible Bioelectronic Implants: Comparison of Different Coating Materials Using Test Methodologies for Life Time Estimation, Micromachines, 13, 4, (2022)
34. Prominski A. et al. Porosity-based heterojunctions enable leadless optoelectronic modulation of tissues, Nature Materials, 21, 647–655 (2022). [PubMed: 35618824]

35. Cummer SA et al. Controlling sound with acoustic metamaterials. Nature Reviews Materials, 1(16001) (2016)
36. Suchowski H. et al. Phase mismatch-free nonlinear propagation in optical zero-index materials, Science, 342, 6163, (2013)
37. Canalias C. and Pasiskevicius V, Mirrorless optical parametric oscillator, Nature Photonics, 1, 459–462, (2007).
38. Shalaev et al. Optical negative-index metamaterials, Nature Photonics, 1, 41–48 (2007).
39. Surjadi J. et al. Mechanical metamaterials and their engineering applications, Advanced Engineering Materials, 21, 3 (2019)
40. Montgomery S. et al. , Magneto-mechanical metamaterials with widely tunable mechanical properties and acoustic bandgaps, Advanced Functional Materials, 31, 3, (2020).
41. Blanton T, International Centre for Diffraction Data, Newtown Square, PA, USA. Private Communication (2014).
42. Liu LG, The Australian National University, Canberra ACT, Australia. Private Communication (1988).
43. Hu JZ et al. Crystal data for high-pressure phases of silicon. Phys. Rev. B: Condens. Matter. Mater. Phys.34, 4679 (1986).
44. Ahmed N, Numerical analysis of transport properties of ZnO based Schottky diode, Phys. Scr 96 (2021)
45. Wang B. et al. , Multichannel power electronics and magnetic nanoparticles for selective thermal magnetogenetics", Journal of Neural Engineering, 19 (2022)

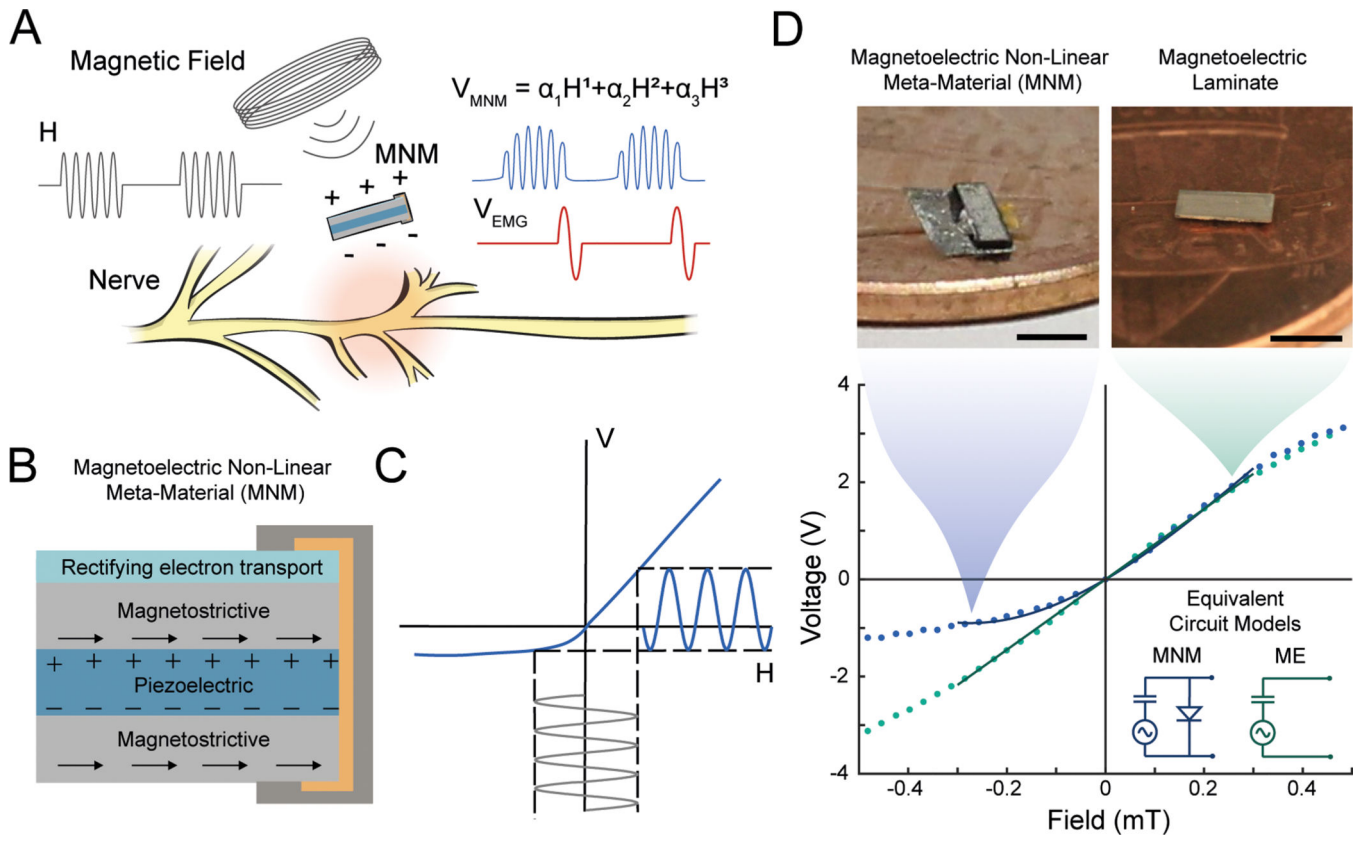

Fig 1. Magnetoelectric Nonlinear Metamaterials Enable Wireless Neuromodulation using Magnetic Fields

(A) Schematic of the remote neural stimulation using a magnetoelectric metamaterial (MNM). Upon applying a pulsed magnetic field, the MNM generates a biased non-linear electric field that is used to stimulate neural tissue. (B) Schematic of the laminate structure of the MNM. The metamaterial consists of a piezoelectric layer between two magnetostrictive layers. A rectifying electron transport (RET) layer sits on top of the stack and includes an electrical connection between the top and bottom surfaces. This additional layer introduces a non-linear Magnetoelectric (ME) coupling coefficient as seen when plotting the relationship between H and V. (C) Conceptual plot of the voltage obtained across the MNM upon application of an AC magnetic field at the mechanical resonant frequency of the material. Note that the nonlinear H-V relationship causes self-rectification of the voltage. (D) Measured magnetic field (B) vs voltage (V - amplitude) curves for representative MNMs (blue) and ME laminates (green) along with a polynomial and a linear fit, respectively. Inset shows the two equivalent circuit models for both the MNM and ME and magnified images of each material is displayed on top (Scale bars = 2 mm; $B = \mu_0 H$, where μ_0 = permeability of free space).

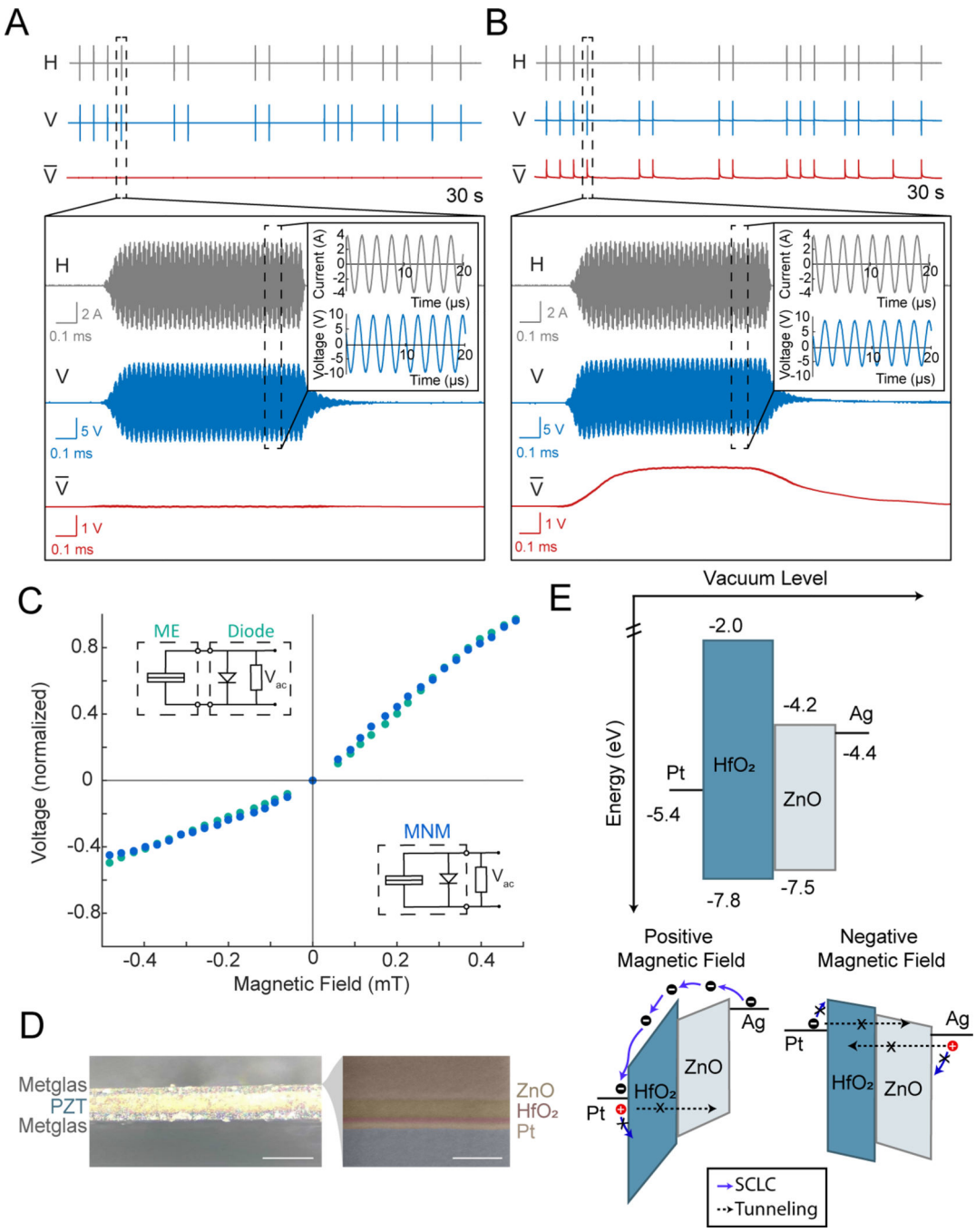

Fig. 2. Arbitrary pulse trains and characterization of the magnetoelectric nonlinear metamaterial

(A & B) Top: Gray lines show an arbitrary pulse train of an applied AC magnetic field (H) at 375 kHz, which matches the mechanical resonant frequency of the ME and MNM films. Here we applied the magnetic field simultaneously to both the ME and MNM from one magnetic field transmitter. We replot the same magnetic field measurement in panels A and B to aid the comparison between the ME and MNM response. Blue lines show the measured voltages from representative ME and MNM materials. The red line shows the voltage resulting from averaging across a 200 μs sliding window of the pulsed voltage waveform.

For the MNM we observe a self-rectification of 1.7 V in the average voltage, but for the ME the average voltage remains near zero. Bottom: Magnified time scales of the pulse trains to show a single pulse. Inset shows further magnification revealing the self-rectifying response in the MNM. All data taken at the fundamental longitudinal resonance modes. (C) Normalized magnetic field (H) vs voltage (V - amplitude) plotted for a ME laminate connected to a RET (green) and for an integrated MNM (blue). The two plots closely follow each other confirming that the nonlinear ME coefficient can be well explained by the altered electronic properties produced by the RET. (D) Optical image of cross section of MNM material. (Scale bar =150 μm) Expanded false-colored SEM image of the RET layers. (Scale bar = 300 nm) (E) Band diagram of the RET layers showing both the forward and reverse biased modes when a positive magnetic field is applied vs a negative field.

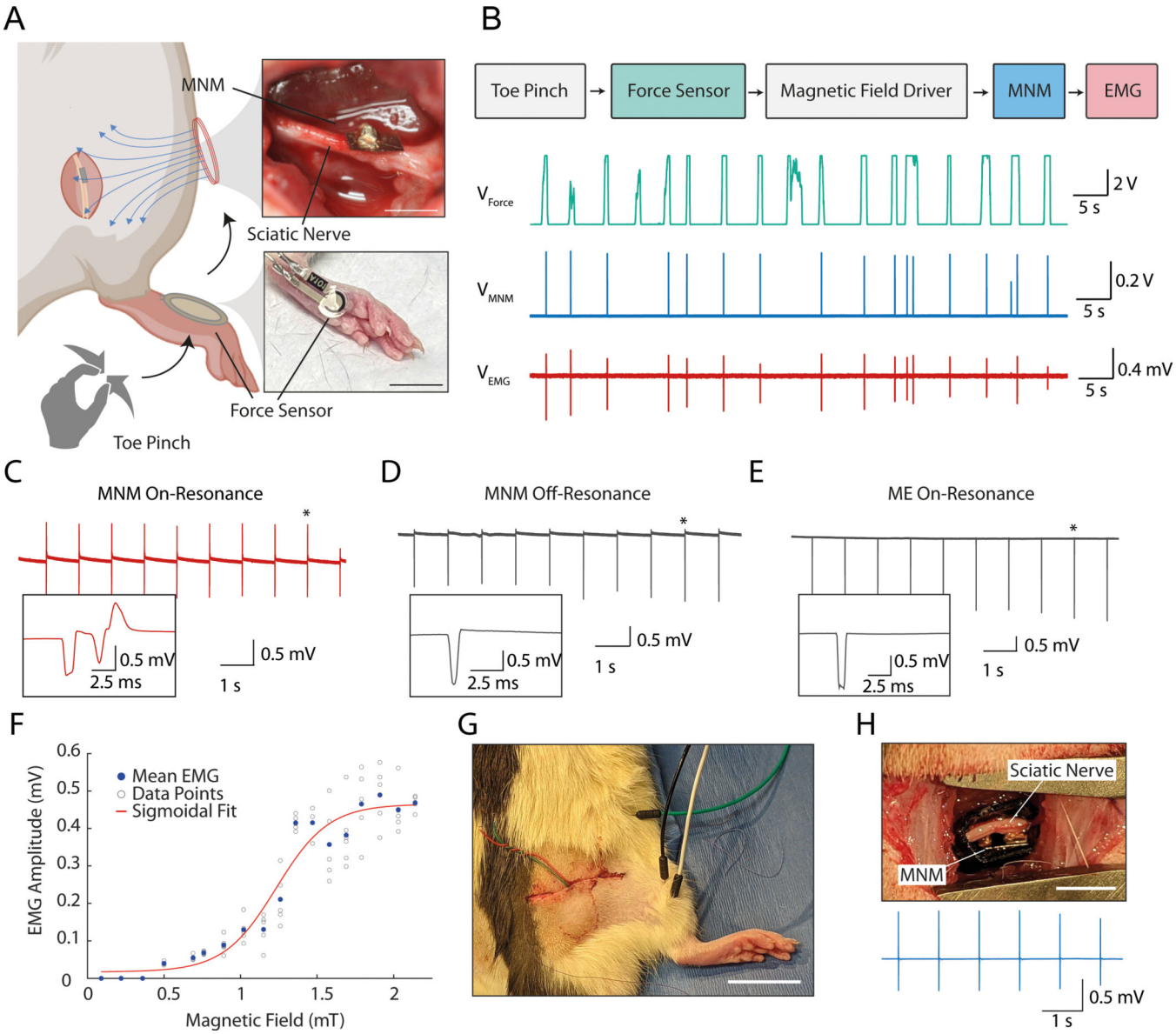

Fig. 3. In Vivo Experiments and Controls using the MNM

(A) Schematic of sensory and reflex restoration based on a toe pinch in an anesthetized rat. Inset images show a representative MNM in contact with the rat sciatic nerve (scale bar = 3 mm) and the force sensor used on the rat foot (scale bar = .1 cm). (B) Flow chart depicting sensory pathway from toe pinch to resulting leg contraction measured by the EMG. Voltage recordings of the force sensor, MNM, and EMG show that arbitrary patterns of toe pinches produce a restored motor reflex. (C) EMG response measured when MNM is driven with a magnetic field at the fundamental longitudinal resonance frequency and pulsing at a periodic 1 Hz. (D) Control experiment shows no measurable EMG response obtained when MNM is driven off-resonance. (E) Second control experiment shows no measurable EMG response when MNM was replaced with similarly sized ME laminate and driven on resonance. (F) Muscle recruitment curve as the applied magnetic field to activate the MNM is varied. (G) Image of closed-wound in vivo model. The MNM is implanted with the nerve clip, and the

feedback wires, excess suture, and EMG leads can be seen. (scale bar = 1 cm) (H) Close-up view of the implanted MNM with nerve clip on the sciatic nerve. Below the image is the recorded EMG from the closed-wound experiment. (scale bar = 3 mm)

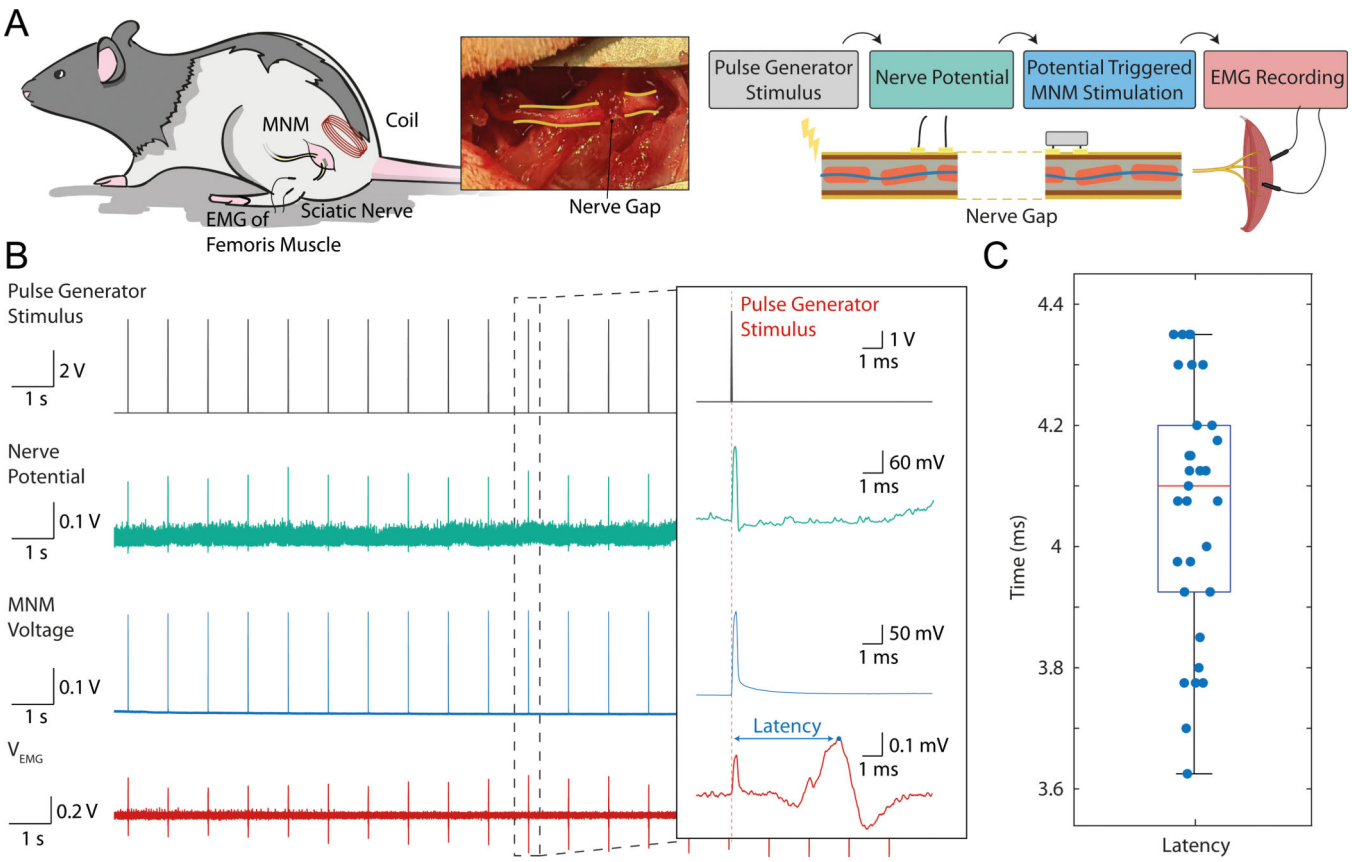

Fig. 4. Measured Stimulation Latency of MNM in a Severed Nerve Rodent Model

(A) Schematic showing how the MNM can support the restoration of nerve conduction across a severed sciatic nerve in vivo. The flow chart and corresponding nerve schematic shows the experimental setup to bridge the nerve gap. A compound nerve action potential is initiated by a pulse generator (PG) and the downstream nerve action potential (NAP) is detected at the proximal nerve end with cuff electrodes. The measurement of the NAP with the cuff electrodes then triggers the application of the magnetic field that drives the MNM in contact with the distal end of the nerve. This in turn stimulates a NAP on the distal side of the nerve thus bridging the nerve gap and activating a muscle response. (B) Voltage recordings on four channels corresponding to the PG stimulus, nerve potential, MNM voltage, and EMG voltage. The inset shows an expanded view of a single bridged nerve signal. (C) Boxplot of the latency of the EMG resulting from the initial PG stimulus across the nerve gap (n = 29 traces counted, maximum = 4.35 ms, minimum = 3.63 ms, median = 4.10 ms, 25th percentile = 3.93 ms, 75th percentile = 4.20 ms).

Table 1.
Engineered material properties in metamaterials.

The Greek characters in this table represent the coefficients used to quantify how a material mediates the relationship between the physical properties listed across the rows and columns of the table. This relationship is described mathematically in the equations below. In the case of metamaterials, these coefficients can be engineered using composite materials and structures. We have color coded these coefficients and equations based on how these metamaterials are referred to in literature. Here, D is the electric displacement, E is the electric field, V_{ME} is voltage, B is the magnetic flux density, H is the magnetic field, d is the thickness of magnetoelectric composite, P is the pressure, V is volume, du/dt is particle velocity, F is force, δ is displacement, dε is the strain. The outlined coefficient α represents the magnetoelectric metamaterial described here. Bolded Greek letters in equations correspond to the ones in the table.